J|A|C|S
ARTICLES

Spin-Selective Charge Transport Pathways through p-Oligophenylene-Linked Donor−Bridge−Acceptor Molecules

Amy M. Scott, Tomoaki Miura, Annie Butler Ricks, Zachary E. X. Dance,
Emilie M. Giacobbe, Michael T. Colvin, and Michael R. Wasielewski*

*Department of Chemistry and Argonne-Northwestern Solar Energy Research (ANSER) Center,
Northwestern University, Evanston, Illinois 60208-3113*

Received September 8, 2009; E-mail: m-wasielewski@northwestern.edu

Abstract: A series of donor−bridge−acceptor (D-B-A) triads have been synthesized in which the donor, 3,5-dimethyl-4-(9-anthracenyl)julolidine (DMJ-An), and the acceptor, naphthalene-1,8:4,5-bis(dicarboximide) (NI), are linked by p-oligophenylene (Ph_n) bridging units ($n = 1-5$). Photoexcitation of DMJ−An produces $DMJ^{+\bullet}−An^{-\bullet}$ quantitatively, so that $An^{-\bullet}$ acts as a high potential electron donor, which rapidly transfers an electron to NI yielding a long-lived spin-coherent radical ion pair ($DMJ^{+\bullet}$-An-Ph_n-$NI^{-\bullet}$). The charge transfer properties of **1−5** have been studied using transient absorption spectroscopy, magnetic field effects (MFEs) on radical pair and triplet yields, and time-resolved electron paramagnetic resonance (TREPR) spectroscopy. The charge separation (CS) and recombination (CR) reactions exhibit exponential distance dependencies with damping coefficients of $\beta = 0.35$ Å^{-1} and 0.34 Å^{-1}, respectively. Based on these data, a change in mechanism from superexchange to hopping was not observed for either process in this system. However, the CR reaction is spin-selective and produces the singlet ground state and both ^{3*}An and ^{3*}NI. A kinetic analysis of the MFE data shows that superexchange dominates both pathways with $\beta = 0.48$ Å^{-1} for the singlet CR pathway and $\beta = 0.35$ Å^{-1} for the triplet CR pathway. MFEs and TREPR experiments were used to measure the spin−spin exchange interaction, $2J$, which is directly related to the electronic coupling matrix element for CR, V_{CR}^2. The magnitude of $2J$ also shows an exponential distance dependence with a damping coefficient $\alpha = 0.36$ Å^{-1}, which agrees with the β values obtained from the distance dependence for triplet CR. These results were analyzed in terms of the bridge molecular orbitals that participate in the charge transport mechanism.

Introduction

Charge transport plays an integral role in many fields including physics, chemistry, and biology and has revolutionized how simple molecular systems with unique photochemical and electronic properties can be utilized as photofunctional materials for solar energy conversion,[1] photocatalysis,[2,3] and optoelectronic nanodevices.[4,5] In particular, there is a great need to develop new, tunable materials that efficiently use light to separate charge and demonstrate distance-independent charge transport. The multistep electron transfer pathway in photosynthetic reaction centers converts photon energy into chemical energy with near unity efficiency using highly ordered assemblies of chromophores to separate charge over distances of 35 Å within these membrane-bound proteins.[6,7] The photogeneration of radical ion pairs (RPs) within reaction center proteins

has inspired the design of organic donor−bridge−acceptor (D-B-A) systems that exhibit efficient, controlled energy and charge transport as a means of capturing solar energy.[8] Charge transport has been studied in covalently linked D-B-A systems with modified bridge molecules, such as proteins,[9] DNA,[10−12] chromophores,[13] saturated[14] and unsaturated phenylene spacers,[15−19] but, often, multiple charge transport pathways exist and the factors that influence them still remain poorly understood. There is a growing effort to understand how the electronic structure and composition of the bridge governs the charge transport mechanism and thus influences the lifetimes of photogenerated RPs ($D^{+\bullet}$-B-$A^{-\bullet}$).[20−25]

The utilization of rigid donors and acceptors with varying bridge lengths allows for the measurement of distance dependent electron transfer rates with the aim of elucidating the superexchange and hopping charge transfer regimes within molecular

(1) Baik, C.; Kim, D.; Kang, M. S.; Kang, S. O.; Ko, J.; Nazeeruddin, M. K.; Gratzel, M. *J. Photochem. Photobiol., A* **2009**, *201* (2−3), 168−174.
(2) Kunkely, H.; Vogler, A. *Angew. Chem., Int. Ed.* **2009**, *48* (9), 1685−1687.
(3) Barber, J. *Chem. Soc. Rev.* **2009**, *38* (1), 185−196.
(4) Straight, S. D.; Andreasson, J.; Kodis, G.; Bandyopadhyay, S.; Mitchell, R. H.; Moore, T. A.; Moore, A. L.; Gust, D. *J. Am. Chem. Soc.* **2005**, *127* (26), 9403−9409.
(5) Flood, A. H.; Stoddart, J. F.; Steuerman, D. W.; Heath, J. R. *Science* **2004**, *306* (5704), 2055−2056.
(6) Wasielewski, M. R. *Chem. Rev.* **1992**, *92*, 435−461.
(7) Parson, W. W. *Science* **2007**, *316* (5830), 1438−1439.

(8) Wasielewski, M. R. *J. Org. Chem.* **2006**, *71* (14), 5051−5066.
(9) Gray, H. B.; Winkler, J. R. *Proc. Natl. Acad. Sci. U.S.A.* **2005**, *102* (10), 3534−3539.
(10) Jortner, J.; Bixon, M.; Langenbacher, T.; Michel-Beyerle, M. E. *Proc. Natl. Acad. Sci. U.S.A.* **1998**, *95*, 12759−12765.
(11) Lewis, F. D.; Wu, T.; Zhang, Y.; Letsinger, R. L.; Greenfield, S. R.; Wasielewski, M. R. *Science* **1997**, *277* (5326), 673−676.
(12) Daublain, P.; Siegmund, K.; Hariharan, M.; Vura-Weis, J.; Wasielewski, M. R.; Lewis, F. D.; Shafirovich, V.; Wang, Q.; Raytchev, M.; Fiebig, T. *Photochem. Photobiol. Sci.* **2008**, *7* (12), 1501−1508.

systems.[10,26−29] Superexchange is the virtual mediation of charge transport from donor to acceptor by bridge orbitals energetically well-separated from those of the donor and acceptor. Charge transfer occurs in a single step with a rate that decays exponentially with distance that is described by the damping factor β. In contrast, sequential charge transport or hopping occurs from the donor to the bridge, as well as between bridge sites. Ultimately, charge trapping occurs at the acceptor whose electron affinity is greater than that of the bridge. Charge hopping by direct injection of charge from the donor to the bridge, and/or between bridge sites, can occur by tunneling through small potential barriers between successive sites,[30−32] or by thermal activation, where the energy barrier between sites is lowered by internal or solvent nuclear reorganization to allow the system to surmount the barriers.[30] Charge transport rates for the hopping mechanism are only weakly distance dependent ($1/r$) allowing charge to move efficiently at long distances, so that systems exhibiting this mechanism are termed "molecular wires".[33−35] Although molecular systems may display a combination of charge transport mechanisms, there are certain criteria that drive photoinduced charge transport in D-B-A systems toward a particular mechanism, such as (1) the magnitude of the donor-to-bridge charge injection barrier as characterized by the energy levels of the system,[36] (2) the energy required for internal and solvent nuclear reorganization, and (3)
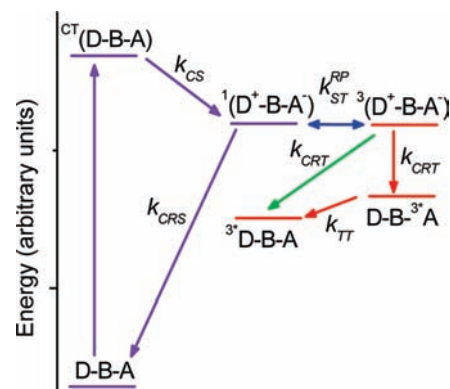

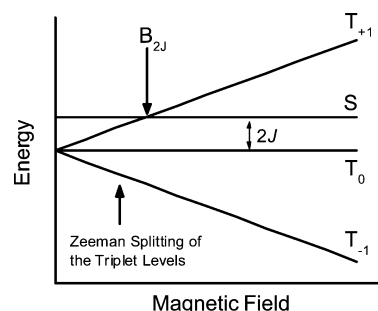**Figure 1.** Charge transfer scheme for **1**−**5**.

Figure 2. Schematic of radical ion pair energy levels as a function of magnetic field ($2J > 0$).

the electronic coupling of the bridge to the donor and acceptor. The overall electronic coupling matrix element, V_{DA}, describes the interaction between the donor and acceptor and is important for determining rates of nonadiabatic charge transfer reactions.[37−40]

For charge recombination (CR), a fourth criterion must be added, that of spin selectivity. The photogenerated singlet RP may undergo electron−nuclear hyperfine coupling-induced radical pair intersystem crossing (RP-ISC) to produce the triplet RP, $^1(D^{+•}\text{-B-A}^{-•}) \rightarrow {}^3(D^{+•}\text{-B-A}^{-•})$. The subsequent CR is spin selective; i.e., the singlet RP recombines to the singlet ground state, and the triplet RP recombines to yield the neutral local triplet (Figure 1). Application of a static magnetic field causes Zeeman splitting of the RP triplet sublevels, and varying the field strength modulates the efficiency of RP-ISC by adjusting the energies of triplet sublevels relative to that of the singlet level (Figure 2). When the Zeeman splitting of the triplet RP sublevels equals the intrinsic singlet−triplet splitting, $2J$, of the RP, there is an increase in the RP-ISC rate. This increase translates into a maximum in triplet RP production and therefore a maximum in neutral local triplet yield upon CR. By monitoring the yield of local triplet production as a function of applied magnetic field, the magnitude of $2J$ can be measured directly[41,42]

(13) Kobori, Y.; Yamauchi, S.; Akiyama, K.; Tero-Kubota, S.; Imahori, H.; Fukuzumi, S.; Norris, J. R., Jr. *Proc. Natl. Acad. Sci. U.S.A.* **2005**, *102* (29), 10017–10022.
(14) Paulson, B. P.; Miller, J. R.; Gan, W. X.; Closs, G. *J. Am. Chem. Soc.* **2005**, *127* (13), 4860–4868.
(15) Lembo, A.; Tagliatesta, P.; Guldi, D. M.; Wielopolski, M.; Nuccetelli, M. *J. Phys. Chem. A* **2009**, *113* (9), 1779–1793.
(16) Albinsson, B.; Mårtensson, J. *J. Photochem. Photobiol., C* **2008**, *9* (3), 138–155.
(17) Wielopolski, M.; Atienza, C.; Clark, T.; Guldi, D. M.; Martin, N. *Chem.−Eur. J.* **2008**, *14* (21), 6379–6390.
(18) Martin, N.; Giacalone, F.; Segura, J. L.; Martin, N.; Guldi, D. M. *Synth. Met.* **2004**, *147* (1−3), 57–61.
(19) Guldi, D. M.; Luo, C.; Swartz, A.; Gomez, R.; Segura, J. L.; Martin, N. *J. Phys. Chem. A* **2004**, *108* (3), 455–467.
(20) Albinsson, B.; Eng, M. P.; Pettersson, K.; Winters, M. U. *Phys. Chem. Chem. Phys.* **2007**, *9* (44), 5847–5864.
(21) Goldsmith, R. H.; Sinks, L. E.; Kelley, R. F.; Betzen, L. J.; Liu, W.; Weiss, E. A.; Ratner, M. A.; Wasielewski, M. R. *Proc. Natl. Acad. Sci. U.S.A.* **2005**, *102* (10), 3540–3545.
(22) Goldsmith, R. H.; Vura-Weis, J.; Scott, A. M.; Borkar, S.; Sen, A.; Ratner, M. A.; Wasielewski, M. R. *J. Am. Chem. Soc.* **2008**, *130* (24), 7659–7669.
(23) Bixon, M.; Jortner, J. *J. Chem. Phys.* **1997**, *107* (13), 5154–5170.
(24) McConnell, H. M. *J. Chem. Phys.* **1961**, *35* (2), 508–515.
(25) Paddon-Row, M. N.; Oliver, A. M.; Warman, J. M.; Smit, K. J.; de Haas, M. P.; Oevering, H.; Verhoeven, J. W. *J. Phys. Chem.* **1988**, *92* (24), 6958–6962.
(26) Lambert, C.; Noll, G.; Schelter, J. *Nat. Mater.* **2002**, *1* (1), 69–73.
(27) Davis, W. B.; Wasielewski, M. R.; Ratner, M. A.; Mujica, V.; Nitzan, A. *J. Phys. Chem.* **1997**, *101*, 6158–6164.
(28) Johnson, M. D.; Miller, J. R.; Green, N. S.; Closs, G. L. *J. Phys. Chem.* **1989**, *93* (4), 1173–6.
(29) Bixon, M.; Jortner, J. *Adv. Chem. Phys.* **1999**, *106*, 3.
(30) Berlin, Y. A.; Burin, A. L.; Ratner, M. A. *Chem. Phys.* **2002**, *275*, 61–74.
(31) Berlin, Y. A.; Burin, A. L.; Ratner, M. A. *J. Phys. Chem. A* **2000**, *104*, 443–445.
(32) Berlin, Y. A.; Hutchison, G. R.; Rempala, P.; Ratner, M. A.; Michl, J. *J. Phys. Chem. A* **2003**, *107* (19), 3970–3980.
(33) Davis, W. B.; Svec, W. A.; Ratner, M. A.; Wasielewski, M. R. *Nature* **1998**, *396*, 60–63.
(34) Weiss, E. A.; Ahrens, M. J.; Sinks, L. E.; Gusev, A. V.; Ratner, M. A.; Wasielewski, M. R. *J. Am. Chem. Soc.* **2004**, *126*, 5577–5584.
(35) Joachim, C.; Vinuesa, J. F. *Europhys. Lett.* **1996**, *33* (8), 635–40.
(36) Samanta, M. P.; Tian, W.; Datta, S.; Henderson, J. I.; Kubiak, C. P. *Phys. Rev. B: Condens. Matter* **1996**, *53* (12), R7626–R7629.

(37) Barbara, P. F.; Meyer, T. J.; Ratner, M. A. *J. Phys. Chem.* **1996**, *100* (31), 13148–13168.
(38) Cave, R. J.; Newton, M. D. *Chem. Phys. Lett.* **1996**, *249* (1,2), 15–19.
(39) Cave, R. J.; Newton, M. D.; Kumar, K.; Zimmt, M. B. *J. Phys. Chem.* **1995**, *99*, 17501–17504.
(40) Roest, M. R.; Oliver, A. M.; PaddonRow, M. N.; Verhoeven, J. W. *J. Phys. Chem. A* **1997**, *101* (27), 4867–4871.
(41) Anderson, P. W. *Phys. Rev.* **1959**, *115* (1), 2–13.
(42) Shultz, D. A.; Fico, R. M., Jr.; Bodnar, S. H.; Kumar, R. K.; Vostrikova, K. E.; Kampf, J. W.; Boyle, P. D. *J. Am. Chem. Soc.* **2003**, *125* (38), 11761–11771.

and can be used to estimate V_{DA} because $2J \propto V_{DA}^2$.[34,43-45] The mechanistic details of the radical pair intersystem crossing mechanism (RP-ISC) and the theory behind the magnetic field effects (MFEs) have been researched extensively[46-49] and applied to many donor−acceptor systems[34,50-57] including biological[58-62] systems.

Time-resolved EPR (TREPR) measurements yield additional information on the spin dynamics of the RPs. If $2J$ and the spin−spin dipolar interaction, D, of the RP are small, S-T$_0$ mixing within $D^{+\bullet}$-B-A$^{-\bullet}$ will result in the formation of a spin-correlated RP (SCRP) that can be recognized by the electron spin polarization pattern of its EPR transitions, i.e., enhanced absorption (A) or emission (E).[63-65] The TREPR spectrum of a SCRP consists of a pair of antiphase doublets centered at the g factors of each radical, where the doublet splitting is determined principally by $2J$ and D, and these four lines are split further by the hyperfine couplings of each radical. Simulation of these spectra yield information critical to understanding the spin dynamics of RPs photogenerated within D-B-A systems, as well as determining the magnitude of $2J$ for systems in which its value is too small to measure accurately by MFE measurements.

We recently reported the results of our investigations into photoinduced charge transport in a D-B-A molecular system, in which the donor, 3,5-dimethyl-4-(9-anthracenyl)julolidine (DMJ-An), and the acceptor, naphthalene-1,8:4,5-bis(dicarboximide) (NI), are linked by p-oligophenylene (Ph$_n$) bridging units (**1**−**4**) (Figure 3) to produce a long-lived spin-coherent RP
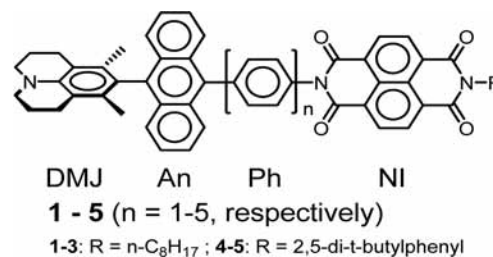
Figure 3. D-B-A molecules used in this study.

(DMJ$^{+\bullet}$-An-Ph$_n$-NI$^{-\bullet}$). Photoexcitation of DMJ-An produces DMJ$^{+\bullet}$-An$^{-\bullet}$ quantitatively, so that An$^{-\bullet}$ acts as a high potential electron donor. Using TREPR spectroscopy at 85 K, we observed a preference for hole transfer over electron transfer[66] for RP recombination to selectively form (DMJ-An-Ph$_n$-^{3*}NI) over (DMJ-^{3*}An-Ph$_n$-NI) for **1**−**4**. The work described here builds significantly upon this initial study and focuses on (1) determining how V_{DA} depends on molecular structure by analyzing the spin−spin exchange interaction ($2J$) between the unpaired spins of the RP as determined by MFEs and TREPR and (2) establishing that the distance dependence of CR in D-B-A molecules is spin-selective using a kinetic model to separate the spin-selective CR rates, k_{CRS} and k_{CRT}, by analyzing MFEs on the observed RP populations as well as the neutral triplet state populations that result from CR.

Experimental Section

The synthesis and characterization of compounds **1**−**4** have been reported,[66] and compound **5** can be found in the Supporting Information. Samples for nanosecond transient absorption spectroscopy were placed in a 10 mm path length quartz cuvette and freeze−pump−thawed five times. The samples were excited with 7 ns, 2.5 mJ, 416 nm using the frequency-tripled output of a Continuum Precision II 8000 Nd:YAG laser pumping a Continuum Panther OPO. The transient absorption spectrum of ^{3*}NI was obtained from a deoxygenated (freeze−pump−thaw) solution of 50:50 toluene:ethyl iodide using 355 nm irradiation.[67] The transient absorption spectra of ^{3*}An and DMJ-^{3*}An were obtained from deoxygenated (freeze−pump−thaw) toluene solutions using 355 nm irradiation. The excitation pulse was collimated to a 5 mm diameter spot and matched to the diameter of the probe pulse generated using a xenon flashlamp (EG&G Electro-Optics FX-200). Kinetic traces were observed from 430−800 nm every 5 nm using a monochromator and photomultiplier tube with high voltage applied to only four dynodes (Hamamatsu R928) and recorded with a LeCroy Wavesurfer 42Xs oscilloscope interfaced to a customized Labview program (Labview v. 8.5.2). The total instrument response time is 7 ns and is determined primarily by the laser pulse duration. Analysis of the kinetic data was performed at multiple wavelengths using a Levenberg−Marquardt nonlinear least-squares fit to a general sum-of-exponentials function with an added Gaussian function to account for the finite instrument response. For the magnetic field effect experiments, the sample cuvette was placed between the poles of a Walker Scientific HV-4W electromagnet powered by a Walker Magnion HS-735 power supply and the field strength was measured by a Lakeshore gaussmeter with a Hall effect probe. The electromagnet and gaussmeter were interfaced with Labview, allowing measurements and control of the magnetic field to $\pm 1 \times 10^{-5}$ T during the data acquisition. To maintain sample integrity during the experiment, a probe light shutter was used to

(43) Kobori, Y.; Sekiguchi, S.; Akiyama, K.; Tero-Kubota, S. *J. Phys. Chem. A* **1999**, *103*, 5416−5424.

(44) Paddon-Row, M. N.; Shephard, M. J. *J. Phys. Chem. A* **2002**, *106* (12), 2935−2944.

(45) Volk, M.; Haberle, T.; Feick, R.; Ogrodnik, A.; Michel-Beyerle, M. E. *J. Phys. Chem.* **1993**, *97* (38), 9831−9836.

(46) Weller, A.; Staerk, H.; Treichel, R. *Faraday Discuss. Chem. Soc.* **1984**, *78*, 271−278.

(47) Hoff, A. J.; Gast, P.; van der Vos, R.; Franken, E. M.; Lous, E. J. *Z. Phys. Chem.* **1993**, *180*, 175−192.

(48) Till, U.; Hore, P. J. *Mol. Phys.* **1997**, *90* (2), 289−296.

(49) Steiner, U. E.; Ulrich, T. *Chem. Rev.* **1989**, *89*, 51−147.

(50) Schulten, K.; Staerk, H.; Weller, A.; Werner, H. J.; Nickel, B. *Z. Phys. Chem.* **1976**, *101* (1−6), 371−390.

(51) Tanimoto, Y.; Okada, N.; Itoh, M.; Iwai, K.; Sugioka, K.; Takemura, F.; Nakagaki, R.; Nagakura, S. *Chem. Phys. Lett.* **1987**, *136* (1), 42−46.

(52) Sakaguchi, Y.; Hayashi, H. *J. Phys. Chem. A* **1997**, *101*, 549−555.

(53) Werner, U.; Kuhnle, W.; Staerk, H. *J. Phys. Chem.* **1993**, *97*, 9280−9287.

(54) Weiss, E. A.; Ratner, M. A.; Wasielewski, M. R. *J. Phys. Chem. A* **2003**, *107* (19), 3639−3647.

(55) Lukas, A. S.; Bushard, P. J.; Weiss, E. A.; Wasielewski, M. R. *J. Am. Chem. Soc.* **2003**, *125*, 3921−3930.

(56) Tadjikov, B.; Smirnov, S. *Phys. Chem. Chem. Phys.* **2001**, *3* (2), 204−212.

(57) Tsentalovich, Y. P.; Morozova, O. B.; Avdievich, N. I.; Ananchenko, G. S.; Yurkovskaya, A. V.; Ball, J. D.; Forbes, M. D. E. *J. Phys. Chem. A* **1997**, *101* (47), 8809−8816.

(58) Blankenship, R. E.; Schaafsma, T. J.; Parson, W. W. *Biochim. Biophys. Acta* **1977**, *461*, 297−305.

(59) Plato, M.; Möbius, K.; Michel-Beyerle, M. E.; Bixon, M.; Jortner, J. *J. Am. Chem. Soc.* **1988**, *110* (22), 7279−85.

(60) van der Vos, R.; Hoff, A. J. *Biochim. Biophys. Acta* **1995**, *1228* (1), 73−85.

(61) Werner, H.-J.; Schulten, K.; Weller, A. *Biochim. Biophys. Acta* **1978**, *502*, 255−268.

(62) Norris, J. R.; Bowman, M. K.; Budil, D. E.; Tang, J.; Wraight, C. A.; Closs, G. L. *Proc. Natl. Acad. Sci. U.S.A.* **1982**, *79*, 5532−5536.

(63) Closs, G. L.; Forbes, M. D. E.; Norris, J. R. *J. Phys. Chem.* **1987**, *91* (13), 3592−3599.

(64) Hore, P. J.; Hunter, D. A.; McKie, C. D.; Hoff, A. J. *Chem. Phys. Lett.* **1987**, *137*, 495−500.

(65) Levanon, H.; Hasharoni, K. *Prog. React. Kinet.* **1995**, *20*, 309−46.

(66) Dance, Z. E. X.; Ahrens, M. J.; Vega, A. M.; Ricks, A. B.; McCamant, D. W.; Ratner, M. A.; Wasielewski, M. R. *J. Am. Chem. Soc.* **2008**, *130* (3), 830−832.

(67) Green, S.; Fox, M. A. *J. Phys. Chem.* **1995**, *99* (40), 14752−14757.

block the sample from irradiation when transient absorption kinetics were not being collected. The triplet yield was monitored at 480 and 430 nm, and kinetic traces were collected in increments of 0.3, 1.5, or 5.0 mT with zero field $\Delta A(B = 0)$ collection after four or five steps. To compensate for possible sample degradation, zero field kinetics were collected during the experiment in four- or five-step increments and plotted and fit with polynomial or linear trend lines. These functions were used to calculate the relative RP yield or triplet yield as a function of applied field strength (B) and plotted as $\Delta A(B)/\Delta A(B = 0)$. The results presented are an average of three or more experiments conducted on separate days with freshly prepared samples in spectrophotometric or freshly distilled ACS-grade toluene. Transient absorption experiments for **4** and **5** were performed at varying concentrations, ranging from OD = 0.30 to 0.05 using 416 nm excitation to ensure that the microsecond time scale electron transfer kinetics monitored only intramolecular processes, not intermolecular processes. The three-dimensional data sets of ΔA vs time and λ were subjected to singular value decomposition and global fitting to obtain the kinetic time constants and their decay associated spectra using Surface Xplorer software.[68]

Femtosecond transient absorption measurements were made either using the 420 nm frequency-doubled output from a regeneratively amplified titanium sapphire laser system operating at 2 kHz or the 400 nm frequency-doubled output from a regeneratively amplified titanium sapphire laser system operating at 1 kHz as the excitation pulse. A white light continuum probe pulse was generated by focusing the IR fundamental into a 1-mm sapphire disk. Detection with a CCD spectrograph has previously been described.[34] The samples were irradiated with $0.5-1.0$ μJ per pulse focused to a 200-μm spot. Samples were placed in a 2-mm path length cuvette, and the total instrument response time for the pump−probe experiment was 180 fs. Transient absorption kinetics were fit to a sum of exponentials with a Gaussian instrument function using Levenberg−Marquardt least-squares fitting. Femtosecond transient absorption kinetic traces for **1−4** have been reported.[66]

For EPR measurements at X-band, toluene solutions of **1−5** ($\sim 10^{-4}$ M) were loaded into quartz tubes (4 mm o.d. × 2 mm i.d.), subjected to five freeze−pump−thaw degassing cycles on a vacuum line (10^{-4} mBar), and sealed using a hydrogen torch. TREPR measurements were made at X-band using continuous wave (CW) microwaves and direct detection on a Bruker E-580 spectrometer. Samples were photoexcited at 416 nm using the output from a frequency tripled, H_2−Raman shifted Nd:YAG laser ($1-2$ mJ/pulse, 7 ns, 10 Hz, QuantaRay DCR-2). The polarization of the laser was set to 54.7° relative to the direction of the static magnetic field to avoid magnetophotoselection effects on the spectra. Following photoexcitation, kinetic traces of the transient magnetization were accumulated under CW microwave irradiation ($6-20$ mW). The field modulation was disabled to achieve a $Q/\pi\nu \approx 30$ ns instrument response function (IRF), where Q is the quality factor of the resonator and ν is the resonant frequency, while microwave signals in emission (e) and/or enhanced absorption (a) were detected in both the real and the imaginary channels (quadrature detection). Sweeping the magnetic field gave 2D spectra versus both time and magnetic field. For each kinetic trace, the signal acquired prior to the laser pulse was subtracted from the data. Kinetic traces recorded at magnetic field values off-resonance were considered background signals, whose average was subtracted from all kinetic traces. The spectra were subsequently phased into a Lorentzian part and a dispersive part, and the former, also known as the imaginary magnetic susceptibility χ'', is presented. Temperatures for experiments were controlled by Oxford Instruments CF935 using liquid N_2.

Results

Steady-State Spectroscopy. The ground-state absorption spectrum of DMJ-An in toluene exhibits a broad charge transfer
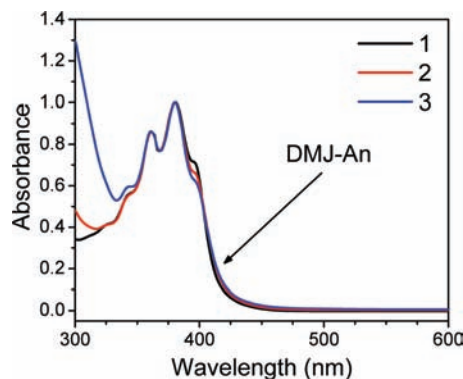
Figure 4. Ground-state UV−vis spectrum of **1−3** in toluene at 295 K.

(CT) absorption maximum at 367 nm with a broad emission maximum at 519 nm, resulting in an excited singlet CT state energy in toluene of 2.89 eV.[66,69] The steady-state absorption spectra of DMJ-An-Ph$_n$-NI for $n = 1-3$ are shown in Figure 4. The absorption maxima at 355 and 325 nm are due to An and NI vibronic bands with an underlying CT absorption band for DMJ-An. The NI electron acceptor has vibronic absorption bands at 343, 363, and 382 nm.[70] The UV band near 300 nm results from absorption of the phenyl bridging unit and increases in intensity with longer bridge lengths. Steady-state fluorescence measurements have been previously reported[66] for **1−4** and show quantum yields for emission $\Phi_{CT} < 0.01$ at room temperature. Molecule **5** has a similarly low emission quantum yield.

Energy Levels and Molecular Structures. Given that photoexcitation of DMJ-An results in quantitative charge separation to produce DMJ$^{+\bullet}$-An$^{-\bullet}$ with a spectroscopically determined energy of 2.89 eV in toluene,[66] the energy levels for the charge separated states, DMJ$^{+\bullet}$-An-Ph$_n$-NI$^{-\bullet}$, DMJ-An-Ph$^{+\bullet}$-NI$^{-\bullet}$, DMJ-An$^{+\bullet}$-Ph$_n$-NI$^{-\bullet}$, and DMJ$^{+\bullet}$-An-Ph$_n$-$^{\bullet}$NI were determined in toluene using eq 1

$$\Delta G_F = \Delta G_I + \text{sign}(E_I - E_F) + \frac{e^2}{\varepsilon_S}\left(\frac{1}{r_I} - \frac{1}{r_F}\right) \quad (1)$$

if $E_F > E_I$ then sign = ($-$), and if $E_I > E_F$ then sign = ($+$). ΔG_I and ΔG_F are the energies above ground state for the initial and final ion pairs, respectively, E_I and E_F are the redox potentials for the initial and final ions, respectively, between which the electron is transferred, r_I and r_F are the initial and final ion pair distances, respectively, e is the electronic charge, and ε_S is the static dielectric constant of the solvent ($\varepsilon_S = 2.38$ for toluene). The distances r_I and r_F between the donor, bridge, and acceptor components were determined from the energy-minimized structures of DMJ-An-Ph$_n$-NI determined with density functional theory (DFT) using Becke's[71] three-parameter hybrid functional with Lee, Yang, and Parr[72] correction functional (B3LYP) and the STO-3G basis set. The redox potentials of DMJ, An, Ph$_n$, and NI are given in the Supporting Information and the ion pair distances and energies are listed in Table S1 and illustrated in Figure 5.

The DFT calculations reveal that the HOMOs of **1−5** are localized on DMJ and the LUMOs are confined to the NI

(68) Surface Xplorer, Ultrafast Systems LLC, Sarasota, FL 34234.

(69) Herbich, J.; Kapturkiewicz, A. *Chem. Phys. Lett.* **1997**, *273*, 9–17.
(70) Greenfield, S. R.; Svec, W. A.; Gosztola, D.; Wasielewski, M. R. *J. Am. Chem. Soc.* **1996**, *118* (28), 6767–6777.
(71) Becke, A. D. *J. Chem. Phys.* **1993**, *98* (2), 1372–1377.
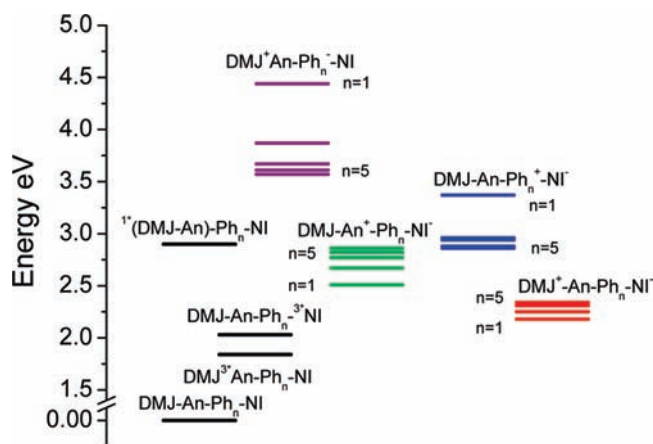(72) Lee, C.; Yang, W.; Parr, R. G. *Phys. Rev. B* **1988**, *37* (2), 785–789.

Figure 5. Energy level diagram for **1**−**5** ion pair states based on eq 1.

acceptor. Energy-minimized structures of the ground state and the corresponding radical ions of DMJ, DMJ-An, An-Ph$_n$, Ph$_n$, and NI were calculated with B3LYP/6-31G*, and the HOMO and LUMO energies are given in Figure S1. The internal reorganization energies, λ_i, were calculated for CR within **1**−**5** by performing a single-point calculation (UHF) B3LYP/6-31G* on the radical ions of the donor, bridge, and acceptors in the DFT-optimized ground state and subtracting the self-consistent field (SCF) energy of the relaxed ionic structure from that of the unrelaxed ground-state structure (Table S2).[73]

Transient Absorption Spectroscopy. Selective photoexcitation into the red edge of the CT absorption band of DMJ-An in toluene at 416 nm results in nearly quantitative formation of ^{1}(DMJ$^{+\bullet}$-An$^{-\bullet}$) with absorption peaks of DMJ$^{+\bullet}$ at 480 nm and An$^{-\bullet}$ at 680 nm in toluene, which decay with $\tau = 45$ ns.[66] The charge separation (CS) reactions, determined by femtosecond transient absorption, of DMJ$^{+\bullet}$-An$^{-\bullet}$-Ph$_n$-NI → DMJ$^{+\bullet}$-An-Ph$_n$-NI$^{-\bullet}$ for **1**−**5** in toluene are very rapid and nearly quantitative. Nanosecond transient absorption was used to extract charge recombination rates (CR) for **1**−**5** in toluene, and the rate constants for these reactions were extracted from the kinetics obtained at the prominent NI$^{-\bullet}$ absorption bands at 480 and 610 nm ($\varepsilon_{480} = 30\,000$ M^{-1}cm^{-1})[70] and are given in Table 1. In comparison, the DMJ$^{+\bullet}$ absorption at 490 nm is weak ($\varepsilon_{max} = 4500$ M^{-1}cm^{-1})[74] and overlaps with that of NI$^{-\bullet}$. The nanosecond transient absorption spectra for **3** are shown in Figure 6A, and the results of singular value decomposition (SVD) analysis with global fitting for **3** are shown in Figure 6B. The spectra for **2**, **4**, and **5** are similar to those of **3** and given in Figure S2. Following rapid CS, the initially formed singlet RP, ^{1}(DMJ$^{+\bullet}$-An-Ph$_n$-NI$^{-\bullet}$), undergoes rapid intersystem crossing induced by electron−nuclear hyperfine coupling within the radicals to produce the triplet RP, ^{3}(DMJ$^{+\bullet}$-An-Ph$_n$-NI$^{-\bullet}$). The energy level of the triplet RP state is above that of ^{3*}An and ^{3*}NI, so that spin-selective CR can occur from the triplet RP to produce (DMJ-An-Ph$_n$-^{3*}NI) ($E_T = 2.03$ eV)[75,76] and (DMJ-

^{3*}An-Ph$_n$-NI) ($E_T = 1.85$ eV).[77] ^{3*}NI and ^{3*}An exhibit broad absorption features at 480 and 430 nm[78] (Figure 6), respectively, which persist on the microsecond time scale and appear as a plateaus in the kinetic traces.

To help understand these transient absorption kinetics, the absorption spectra of ^{3*}NI and ^{3*}An were compared to that of DMJ-^{3*}An, which forms in appreciable amounts upon CR of ^{1}(DMJ$^{+\bullet}$-An$^{-\bullet}$).[79] The ^{3*}NI and ^{3*}An absorption spectra were normalized, added, and overlaid with the nanosecond transient absorption spectrum of **3** acquired 1.5 μs after the excitation pulse (Figure S2E). The spectra are qualitatively identical and confirm that ^{3*}An and ^{3*}NI species both form at 295 K upon CR (Figures 6 and S2A-C). This behavior contrasts with that observed at 85 K, where ^{3*}NI forms initially and is followed by triplet−triplet energy transfer (TEnT) to yield ^{3*}An.[66] (see Discussion). The kinetics at the 430 nm ^{3*}An absorption exhibit a plateau lasting into the microsecond regime. While the ^{3*}An absorption overlaps with those of NI$^{-\bullet}$ and ^{3*}NI, the extinction coefficient of ^{3*}An ($\varepsilon = 42\,000 \pm 4000$ M^{-1} cm^{-1}) at 430 nm is considerably larger those of NI$^{-\bullet}$ and ^{3*}NI,[80] so that the analysis of the 430 nm kinetic traces monitor the concentration of ^{3*}An reasonably well.

The transient absorption spectra for **1** exhibit a weak 430 nm band, and the kinetics show a long-lived plateau with a rise time of 7 ns, which is within the instrument response function. The corresponding spectra for **2**−**4** show transient decays of NI$^{-\bullet}$ at 480 nm having lifetimes that match the appearance kinetics for ^{3*}An at 430 nm. For example, the 480 nm decay of NI$^{-\bullet}$ for **3** occurs with $\tau = 345 \pm 4$ ns and is within experimental uncertainty of the 340 ± 6 ns rise at 430 nm attributed to ^{3*}An (Figure S3). This confirms that ^{3*}An is generated upon the CR of DMJ$^{+\bullet}$-An-Ph$_n$-NI$^{-\bullet}$, as opposed to being produced by CR from the initial ion pair state, (DMJ$^{+\bullet}$-An$^{-\bullet}$). This is expected because the reaction DMJ$^{+\bullet}$-An$^{-\bullet}$-Ph$_n$-NI → DMJ$^{+\bullet}$-An-Ph$_n$-NI$^{-\bullet}$ occurs on a subnanosecond time scale and is considerably faster than the 45 ns decay time of ^{1}(DMJ$^{+\bullet}$-An$^{-\bullet}$) that leads to about a 45% yield of DMJ-^{3*}An.[79] Further evidence indicating that CR produces both ^{3*}NI and ^{3*}An is derived from the decay-associated spectra (Figure 6B), which reveal two major components with absorption features consistent with the decay of NI$^{-\bullet}$ and simultaneous rise of ^{3*}NI and ^{3*}An. The species-associated time constants for NI$^{-\bullet}$ decay are very similar to those obtained by fitting the individual kinetics (Table 1). The spectra for **1**−**5** also show that the ^{3*}An yield is greater for **3** and **4** having the longer bridges relative to that for **1** and **2** having the shorter bridges. The transient absorption signal for **5** at 430 nm is small in comparison to those of **1**−**4** because the sample concentration is much lower, so that diffusion leading to intermolecular CR does not contribute to the electron transfer rate analysis.

Magnetic Field Effect and TREPR Experiments. The MFE experiments that directly measure the magnitude of the spin−spin exchange interaction, $2J$, were performed at room temperature for **1**−**4** in toluene, and the magnetic field dependence of the DMJ-An-Ph$_n$-^{3*}NI yields formed by RP-ISC are shown for **1**

(73) Weiss, E. A.; Tauber, M. J.; Kelley, R. F.; Ahrens, M. J.; Ratner, M. A.; Wasielewski, M. R. *J. Am. Chem. Soc.* **2005**, *127* (33), 11842–11850.

(74) Okada, T.; Fujita, T.; Kubota, M.; Masaki, S.; Mataga, N.; Ide, R.; Sakata, Y.; Misumi, S. *Chem. Phys. Lett.* **1972**, *14* (5), 563–568.

(75) Wiederrecht, G. P.; Svec, W. A.; Wasielewski, M. R.; Galili, T.; Levanon, H. *J. Am. Chem. Soc.* **2000**, *122* (40), 9715–9722.

(76) Ganesan, P.; Baggerman, J.; Zhang, H.; Sudhoelter, E. J. R.; Zuilhof, H. *J. Phys. Chem. A* **2007**, *111* (28), 6151–6156.

(77) Langelaar, J.; Rettschnick, R. P. H.; Hoijtink, G. J. *J. Chem. Phys.* **1971**, *54* (1), 1–7.

(78) Livingston, R.; Tanner, D. W. *Trans. Faraday Soc.* **1958**, *54* (6), 765–771.

(79) Dance, Z. E. X.; Mickley, S. M.; Wilson, T. M.; Ricks, A. B.; Scott, A. M.; Ratner, M. A.; Wasielewski, M. R. *J. Phys. Chem. A* **2008**, *112* (18), 4194–4201.

(80) Compton, R. H.; Grattan, K. T. V.; Morrow, T. *J. Photochem.* **1980**, *14* (1), 61–66.

Table 1. Rate Constants for CS (k_{CS}) and CR (k_{CR}), the Spin−Spin Exchange Interaction ($2J$) Measured by MFE and TREPR, and the Rate Constants for CR to the Ground State (k_{CRS}) and to the Triplet State (k_{CRT}) Determined from the MFE Data

compd	k_{CS} (s^{-1})	k_{CR} (s^{-1})^a	k_{CR} (s^{-1})^b	$2J_{MFE}$ (mT)	k_{CRS} (s^{-1})^d	k_{CRT} (s^{-1})^d
1	1.5×10^{11} (± 0.3)	1.3×10^8 (± 0.4)	1.3×10^8 (± 0.4)	170 ± 1	1.1×10^{8e}	9.6×10^{7e}
2	5.0×10^{10} (± 0.5)	8.9×10^6 (± 0.01)	8.1×10^6	30 ± 1	6.8×10^6 (± 0.5)^f	1.5×10^7 (± 0.2)^f
3	1.0×10^{10} (± 0.05)	2.9×10^6 (± 0.04)	2.9×10^6	5.7 ± 1	1.1×10^6 (± 0.1)^g	3.8×10^6 (± 0.2)^g
4	1.7×10^9 (± 0.1)	7.1×10^5 (± 0.4)	7.5×10^5	0.3 ± 0.2^c	2×10^5	1.0×10^6
				0.9 ± 0.1		
5	4.5×10^8 (± 0.3)	2.7×10^5 (± 0.3)	2.7×10^5	0.4 ± 0.1^c	−	−

^{a} CR rate constant measured by transient absorption kinetics monitoring NI$^{-\bullet}$ decay at $B = 0$ mT. ^{b} CR species associated rate constant. ^{c} Measured by TREPR. ^{d} Determined from the kinetic analysis of the MFE data using $k_{hfc} = 1 \times 10^8$ s^{-1}. ^{e} For the fitting, $k_{rlx} \ll 1 \times 10^8$ s^{-1}. ^{f} For the fitting, $k_{rlx} = 1.1 \times 10^6$ (± 0.5) s^{-1}. ^{g} For the fitting, $k_{rlx} = 2.5 \times 10^6$ (± 0.8) s^{-1}.
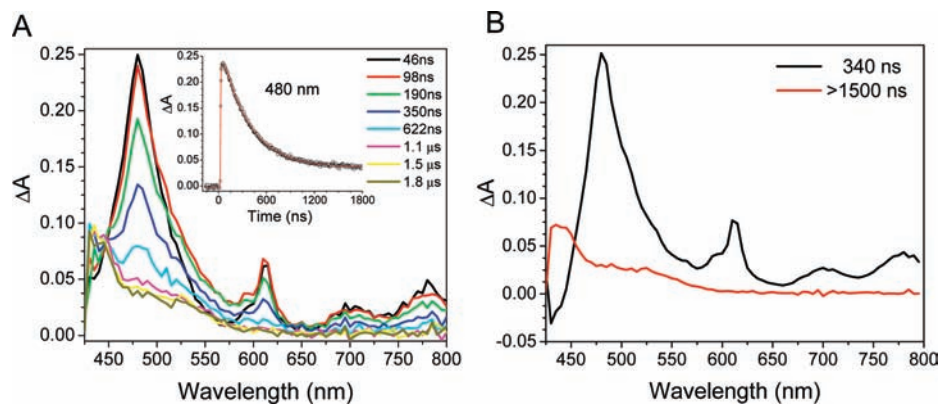

Figure 6. (A) Nanosecond transient absorption spectra of **3** in toluene at 295 K at the indicated times following a 7 ns, 416 nm laser pulse. Inset: transient absorption kinetics of **3** in toluene at 295 K at 480 nm following a 7 ns, 416 nm laser pulse. Data points obtained every 5 nm. (B) Decay-associated spectra and time constants of **3** obtained by global analysis of the transient absorption data.
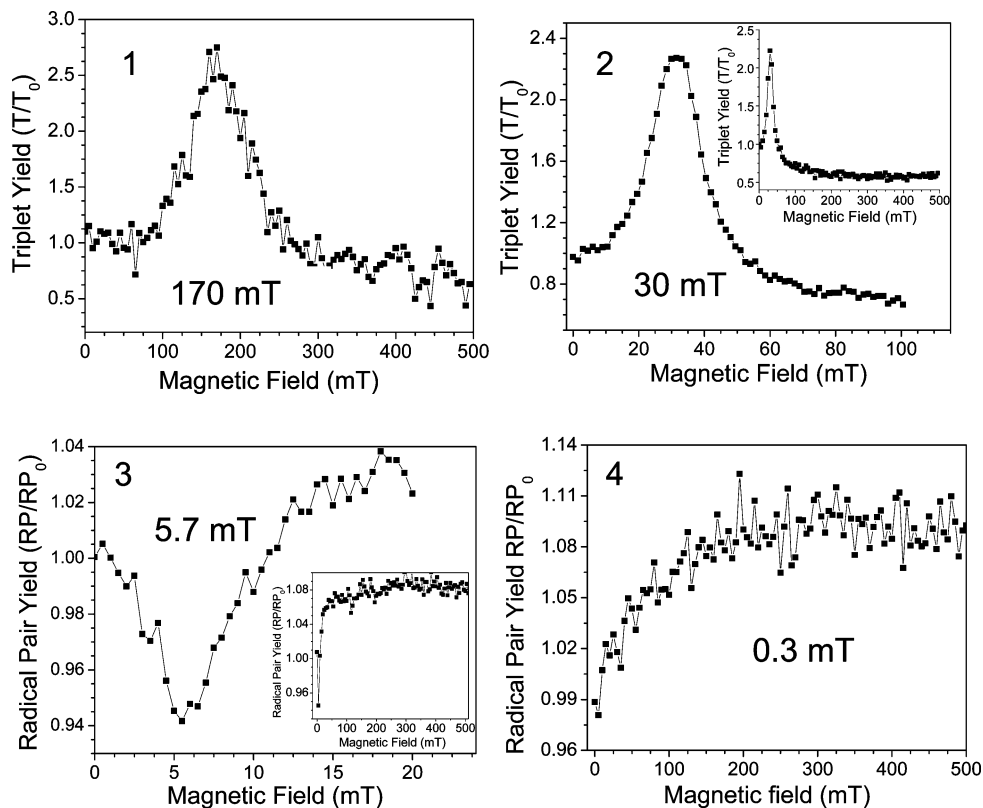
Figure 7. Triplet and radical pair yields as a function of magnetic field (mT) for **1**−**4** in toluene at 480 nm at 295 K (130 ns delay for **3** and 860 ns delay for **4**). The insets show larger magnetic field ranges.

and **2**, Figure 7. The $2J$ values for **1** and **2** decrease from 170 ± 1 mT to 30 ± 1 mT, respectively, and show similar relative triplet yields at 480 nm. The RP yield versus magnetic field plots measured at 480 nm are displayed for **3** and **4** with $2J$ resonances at 57 ± 1 mT and 3 ± 1 mT, respectively, Figure 7. The maximum of the relative triplet yield plot, or minimum
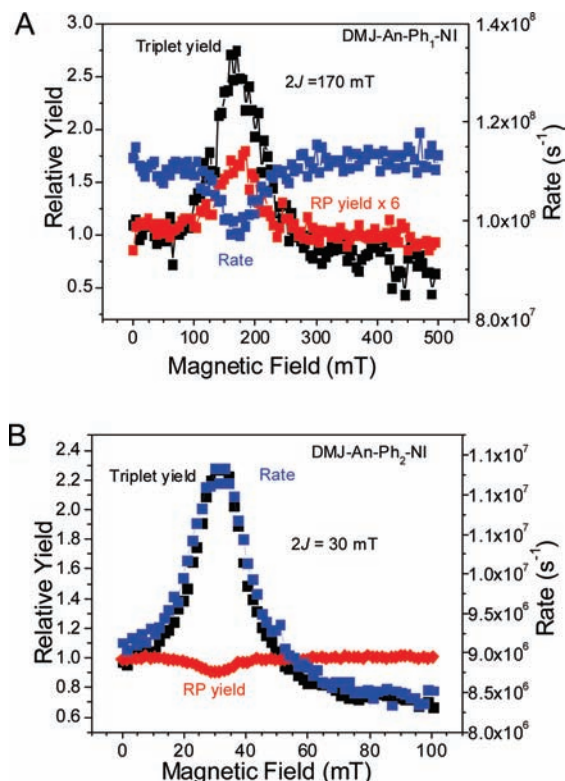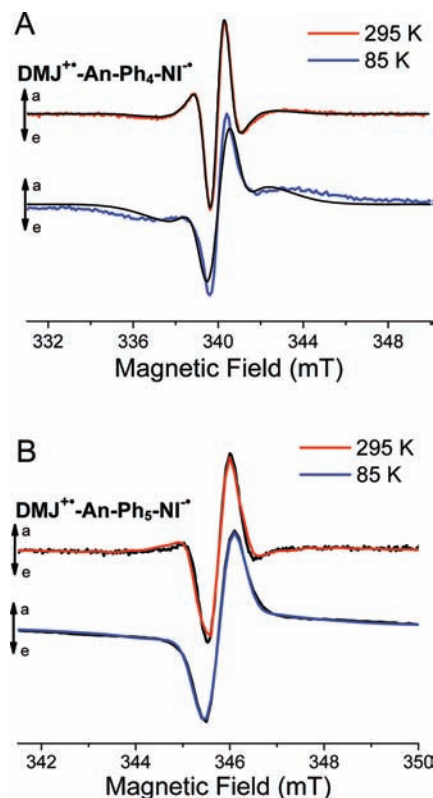
Figure 8. Relative triplet yield, radical pair yield, and charge recombination rate versus magnetic field for (A) **1** in toluene (75 ns delay after the laser pulse for the RP) and (B) **2** in toluene (29 ns delay after the laser pulse for the RP) at 480 nm.

of the relative RP yield plot correspond to the field at which the S and T_{+1} (if $2J > 0$) or T_{-1} (if $2J < 0$) RP energy levels cross. The magnitude of $2J$ is too small in compound **5** to be accurately measured by MFE, so that TREPR experiments were used to determine it. The magnetic field dependence of the triplet yields of DMJ-^{3*}An-Ph$_n$-NI measured at 430 nm are nearly identical to those determined at 480 nm and are shown for **2** (n = 2) in Figure S4.

Figure 8A,B shows plots of the relative RP and triplet yields as well as the CR rates versus magnetic field for **1** and **2** in toluene, respectively. These data qualitatively reveal for **1** that the singlet CR pathway dominates and the total CR rate decreases with increased triplet yield at the resonance condition. Using the same analysis for **2**, the opposite case is observed, and the triplet CR pathway is more efficient than the singlet CR pathway because both the total CR rate and the relative triplet yield increase at the $2J$ resonance, while the RP yield is minimized at resonance. The dominant recombination pathways for **3** and **4** are similar to that of **2** and also show the rate and triplet yield increases at resonance, while the RP yields decrease (see Discussion).

Photoexcitation of **2**−**5** at 416 nm yields spin-polarized RPs at both 295 and 85 K, indicating that charge transfer followed by RP-ISC occurs at both temperatures. Figure 9 shows the TREPR spectra of the RPs formed in **4** and **5** at 295 and 85 K in toluene. The RP lifetime for **1** is too short to observe by

(81) Adrian, F. J. *J. Chem. Phys.* **1972**, *57* (12), 5107–5113.
(82) Atherton, N. M.; Davies, A. G. *Chem. Soc. Rev.* **1993**, *22* (5), U293–U293.
(83) Dance, Z. E. X.; Mi, Q.; McCamant, D. W.; Ahrens, M. J.; Ratner, M. A.; Wasielewski, M. R. *J. Phys. Chem. B* **2006**, *110* (50), 25163–25173.

Figure 9. TREPR spectra of (A) DMJ$^{+•}$-An-Ph$_4$-NI$^{−•}$ at 300 ns, (B) DMJ$^{+•}$-An-Ph$_5$-NI$^{−•}$ at 400 ns, following a 416 nm, 1.5 mJ laser pulse at the indicated temperatures in toluene. Smooth curves superimposed on the experimental spectra are computer simulations of the radical pair spectra (see text) with the parameters given in Table 2. Positive features are in enhanced absorption, while negative features are in emission.

Table 2. Exchange and Dipolar Interaction Parameters

| compd	temp (K)	2J (mT)	D (mT)
4[a]	295	0.86 ± 0.05	−
	85	0.80 ± 0.05	-0.18 ± 0.05
5[b]	295	0.37 ± 0.05	−
	85	0.28 ± 0.05	-0.12 ± 0.05

[a] TREPR spectra obtained 300 ns after the laser pulse. [b] TREPR spectra obtained 400 ns after the laser pulse.

TREPR. The RP spectra of **4** and **5** were simulated with the SCRP mechanism using the model of Till and Hore.[48] The best fits to the data (Figure 9) used the parameters that are summarized in Table 2. The calculated hyperfine coupling constants of DMJ$^{+•}$-An, as well as the measured g-factor and hyperfine coupling constants of NI$^{−•}$ were used in the simulations.[66] The electron spin polarization pattern of the EPR signal, i.e., which transitions are in enhanced absorption (A) or emission (E), is determined by the SCRP sign rule,

$$\Gamma = \mu \times \text{sign}[J - D(3\cos^2(\xi) - 1)] = \\ (-1) \text{ gives } E/A \text{ or } = (+1) \text{ gives } A/E \quad (2)$$

where μ is −1 or +1 for a singlet or triplet excited state precursor, respectively, ξ is the angle between the dipolar axis of the radical pair and the direction of the magnetic field B_0, and D is the dipolar interaction between the two spins. Given that photoexcitation initially produces a singlet RP, and that the experimentally determined absolute phases of the RP spectra are E/A,[81,82] it follows from eq 2 that $2J$ is positive for the RPs at all temperatures. The dipolar interaction (D) between the
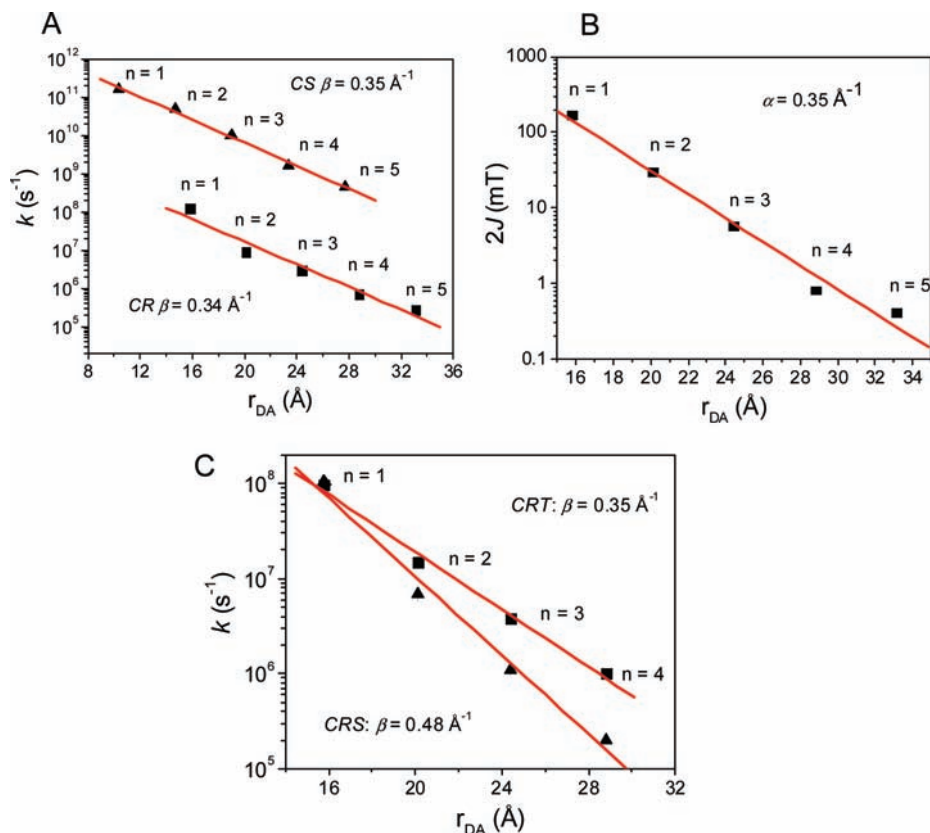
Figure 10. (A) Plots of k_{CS} (■), k_{CR} (▲) at 295 K vs distance, r_{DA}. The red lines are the linear fits to the data. (B) Logarithmic plot of the spin−spin exchange interaction, $2J$, versus distance r_{DA}. (C) Plot of k_{CRT} (■), k_{CRS} (▲) at 295 K vs distance, r_{DA}. The error bars on the data points are smaller than the size of the symbols for all plots.

electron spins in **2−5** is averaged out at room temperature by molecular rotations and was estimated at 85 K from the simulations (Table 2). The experimental details of the absolute phase determination have been described previously.[83]

Our previous TREPR measurements[66] on **1−4** at 85 K show that CR within ³(DMJ⁺•-An-Ph$_n$-NI⁻•) results in the preferential formation of DMJ-An-Ph$_n$-³*NI followed by exponentially distance dependent TEnT in the range of $10^3−10^6$ s⁻¹ to yield DMJ-³*An-Ph$_n$-NI. TEnT has been shown to occur by an exchange mechanism that depends exponentially on the distance between the donor and acceptor.[84−86] The transient absorption data at 295 K presented here show that (DMJ-An-Ph$_n$-³*NI) and (DMJ-³*An-Ph$_n$-NI) are both derived from CR within ³(DMJ⁺•-An-Ph$_n$-NI⁻•) with a total rate of k_{CRT}; however, the TEnT rates for **1−5** cannot be determined readily at 295 K due to bimolecular annihilation in fluid solution.

Discussion

Superexchange-Mediated Charge Transport. The CS and CR rate constants for **1−5** (Figure 10A) decay exponentially with donor−acceptor distance as described by eq 3

$$k = k_0 e^{-\beta(r-r_0)} \tag{3}$$

where k_0 is the rate constant at the van der Waals contact distance r_0 (3.5 Å), and the measured value of $\beta = 0.35$ Å⁻¹ for CS and 0.34 Å⁻¹ for CR. This behavior is characteristic

of the superexchange mechanism in which the β values depend on both the electronic coupling matrix element for the charge transfer process, V_{DA}, as well as the energy gap for charge injection from the donor to the virtual bridge state, ΔE_{DB},[24,87]

$$V_{DA} = \frac{V_{DB} V_{BA}}{\Delta E_{DB}} \left(\frac{V_{BB}}{\Delta E_{DB}} \right)^{N-1} \tag{4}$$

where β is described by

$$\beta = \frac{2}{r} \ln \left(\frac{\Delta E_{DB}}{V_{BB}} \right) \tag{5}$$

and where V_{DB} and V_{BA} are the matrix elements that couple the donor to the bridge and the bridge to the acceptor, respectively, V_{BB} is the electronic coupling between bridge sites, N is the number of identical bridge sites, and r is the length of one bridge segment. Equation 4 is approximate and does not take into account non-nearest neighbor interactions and multiple pathways.[88]

Since the redox potentials for most conjugated bridge molecules, including p-oligophenylenes, depend on bridge length, the charge injection energy gap is also distance dependent. As the bridge length increases, the energy gap may become

(84) Dexter, D. L. *J. Chem. Phys.* **1953**, *21*, 836–50.
(85) Closs, G. L.; Piotrowiak, P.; MacInnis, J. M.; Fleming, G. R. *J. Am. Chem. Soc.* **1988**, *110* (8), 2652–3.
(86) Closs, G. L.; Johnson, M. D.; Miller, J. R.; Piotrowiak, P. *J. Am. Chem. Soc.* **1989**, *111* (10), 3751–3.
(87) Ratner, M. A. *J. Phys. Chem.* **1990**, *94* (12), 4877–4883.
(88) Onuchic, J. N.; Deandrade, P. C. P.; Beratan, D. N. *J. Chem. Phys.* **1991**, *95* (2), 1131–1138.

sufficiently small to allow oxidation or reduction of the bridge, so that crossover from a superexchange to a charge hopping mechanism may occur. The data presented here for DMJ-An-Ph$_n$-NI do not show a switch in mechanism to the charge hopping regime even at longer bridge distances, contrary to what we observed earlier when *p*-oligophenylenes ($n = 1-5$) are linked to a phenothiazine (PTZ) donor and a perylene-3,4:9,10-bis(dicarboximide) (PDI) electron acceptor. The PTZ-Ph$_n$-PDI series shows a change in mechanism from superexchange to hopping for CS at $n = 5$ and CR at $n = 4$.[34] In the CS process, hole injection from ^{1*}PDI into the Ph$_5$ bridge forms PTZ-Ph$_5^{+\bullet}$-PDI$^{-\bullet}$, while for the corresponding CR process, hole transfer from PTZ$^{+\bullet}$ to Ph$_4$ or Ph$_5$ forms the same type of intermediate. This is a consequence of the increased ease of *p*-oligophenylene bridge oxidation for longer bridges and the increased RP energy of PTZ$^{+\bullet}$-Ph$_n$-PDI$^{-\bullet}$ resulting from Coulomb destabilization as n becomes larger. In contrast, CS within the DMJ-An-Ph$_n$-NI series by the hopping mechanism requires reduction of the bridge, DMJ$^{+\bullet}$-An$^{-\bullet}$-Ph$_n$-NI $\rightarrow$ DMJ$^{+\bullet}$-An-Ph$_n^{-\bullet}$-NI, which is least endoergic for $n = 5$ at $\Delta G = 0.68$ eV (Table S1). The corresponding CR reaction may involve either bridge oxidation, DMJ$^{+\bullet}$-An-Ph$_n$-NI $\rightarrow$ DMJ-An-Ph$_n^{+\bullet}$-NI$^{-\bullet}$ or bridge reduction, DMJ$^{+\bullet}$-An-Ph$_n$-NI$^{-\bullet}$ $\rightarrow$ DMJ$^{+\bullet}$-An-Ph$_n^{-\bullet}$-NI. When $n = 5$, the free energies for bridge oxidation and reduction are $\Delta G = 0.59$ and 1.20 eV, respectively (Table S1). Thus, the charge hopping mechanism for both CS and CR is precluded on thermodynamic grounds, so that both reactions are expected to proceed exclusively by the superexchange mechanism.

The relationship between V_{DA} and the spin–spin exchange interaction, $2J$, between the singlet and triplet RP states was originally proposed by Kramers[89] and developed further by Anderson.[41,90] The magnitude and sign of $2J$ depends on the interactions of these states with other energetically nearby states having the same respective spin multiplicities.[41,90] For the CR reaction, an approximate relationship between $2J$ and the electronic coupling matrix elements for the singlet and triplet pathways, V_{CRS} and V_{CRT}, respectively, is given by eq 6[43,54,91]

$$2J = \frac{V_{CRT}^2}{\Delta G_{CRT} + \lambda} - \frac{V_{CRS}^2}{\Delta G_{CRS} + \lambda} \qquad (6)$$

where ΔG_{CRT} and ΔG_{CRS} are the free energies for charge recombination to the triplet and singlet RPs, respectively, and λ is the total reorganization energy for CR given by $\lambda = \lambda_i + \lambda_s$ where λ_i is the internal reorganization energy for CR and λ_s is the solvent reorganization energy. The value of λ is assumed to be spin independent. The value of $2J$ depends exponentially on the distance between two radical ions and is described by[92]

$$2J = 2J_0 e^{-\alpha(r-r_0)} \qquad (7)$$

where $2J_0$ is the spin–spin exchange interaction at the van der Waals contact distance r_0 of 3.5 Å and α is a constant. Figure 10B shows a plot of $2J$ vs distance that yields the distance decay parameter, $\alpha = 0.36$ Å^{-1}, which according to eq 6 directly monitors the decay of the superexchange interaction through the *p*-oligophenylene bridge. Interestingly, the $2J$ values ob-

Table 3. Comparison of Ion Pair Distances and Values of $2J$

	r_{DA} (Å)		$2J$ (mT)	
n	DMJ$^{+\bullet}$-An-Ph$_n$-NI$^{-\bullet}$	PTZ$^{+\bullet}$-Ph$_n$-PDI$^{-\bullet}$	DMJ$^{+\bullet}$-An-Ph$_n$-NI$^{-\bullet}$	PTZ$^{+\bullet}$-Ph$_n$-PDI$^{-\bullet}$
1	16.5	12.8	170	−
2	20.9	17.1	31	170
3	25.5	21.4	5.7	31
4	29.9	25.7	0.9	6.4
5	34.3	30.0	0.4	1.5

tained for the DMJ-An-Ph$_n$-NI series are nearly identical to the $2J$ values measured for the PTZ-Ph$_n$-PDI series for the same D−A distances and both decay exponentially with distance to give $\alpha = 0.36$ Å^{-1} and 0.37 Å^{-1}, respectively, which indicates that the donor−acceptor coupling in these two *p*-oligophenylene systems is similar. For the DMJ-An-Ph$_n$-NI series, the α value also closely matches the β value, which is reasonable given that electron transfer theory shows that $k_{CR} \propto V_{CR}^2$,[93,94] while eq 6 shows that $2J \propto V_{CR}^2$ implying that the prevalent charge transport pathways in the DMJ-An-Ph$_n$-NI system involve only superexchange.

Bridge Structure and Charge Recombination Dynamics. An important aspect of analyzing the effect of the bridge properties on the CR rate is to determine whether An serves as essentially another phenyl group in the bridge or its extended π system has a more significant influence on the bridge properties. Our TREPR studies indicate that the radical cation spin density for DMJ$^{+\bullet}$-An-Ph$_n$-NI$^{-\bullet}$ is confined within DMJ with no delocalization onto An. The ion pair energies calculated using eq 1 (Figure 5) are consistent with this observation because they show that DMJ-An$^{+\bullet}$-Ph$_n$-NI$^{-\bullet}$ is at least 0.33 eV above the fully charge separated DMJ$^{+\bullet}$-An-Ph$_n$-NI$^{-\bullet}$ state ($n = 1$, Figure 5) and is thus a virtual state with respect to the CR reaction. Experimental evidence along with electronic structure calculations on conjugated bridges show that V_{DA} for donors and acceptors attached to the 9- and 10-positions of An is significantly smaller than that for the corresponding Ph bridges largely because steric hindrance provided by the peri-hydrogen atoms adjacent to the 9- and 10-positions of An results in large dihedral angles between the relevant π systems.[95] An analysis of the An-Ph dihedral angles compared to those of Ph-Ph within the *p*-oligophenylene bridges reveals larger dihedral angles for the An-Ph connection, Figure S5.

A comparison between the electronic coupling matrix elements for superexchange charge transfer through Ph$_n$ and An-Ph$_n$ can be made by examining the measured $2J$ values for CR in the DMJ$^{+\bullet}$-An-Ph$_n$-NI$^{-\bullet}$ and PTZ$^{+\bullet}$-Ph$_n$-PDI$^{-\bullet}$ series (Table 3). Note that the donor−acceptor distances for the molecules having the An-Ph$_n$ bridges are nearly the same as those for the molecules having Ph$_{n+1}$ bridges. Interestingly, the $2J$ values for CR within molecules having the An-Ph$_n$ bridges are very similar to those for the molecules having Ph$_{n+1}$ bridges. These data strongly suggest that the superexchange interaction is propagated through the An-Ph$_n$ molecule in a manner similar to the Ph$_{n+1}$ molecule. The presence of the extended π system within An does not increase the coupling, and the influence of the σ bonds that directly link An and Ph should be considered. Recent studies of charge transfer rates through a series of benzoannulated

(89) Kramers, H. A. *Physica* **1934**, *1*, 182–192.
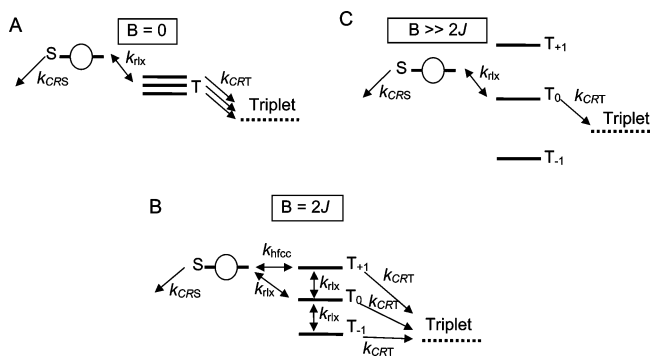(90) Anderson, P. W. *Phys. Rev.* **1950**, *79* (2), 350–356.
(91) Nelsen, S. F.; Ismagilov, R. F.; Teki, Y. *J. Am. Chem. Soc.* **1998**, *120*, 2200–2201.
(92) Kanter, F. J. J. D.; Kaptein, R.; Vansanten, R. A. *Chem. Phys. Lett.* **1977**, *45* (3), 575–579.

(93) Marcus, R. A. *J. Chem. Phys.* **1965**, *43*, 679–701.
(94) Jortner, J. *J. Chem. Phys.* **1976**, *64* (12), 4860–4867.
(95) Lambert, C.; Risko, C.; Coropceanu, V.; Schelter, J.; Amthor, S.; Gruhn, N. E.; Durivage, J. C.; Bredas, J. L. *J. Am. Chem. Soc.* **2005**, *127* (23), 8508–8516.

Figure 11. Kinetic model of RP spin dynamics for CR in **2** and **3** for (A) $B = 0$, (B) $B = 2J$, and (C) $B \gg 2J$. S, T_{+1}, T_0, and T_{-1} denote corresponding RP spin sublevels. The dotted line represents the lowest excited triplet state whose actual energy is far below that of the RP energy levels. The circle indicates that the initial population is located on the singlet RP.

bicyclo[2.2.2]octanes show that weakly coupled π pathways do not increase electron transfer rates and that the dominant pathway for charge transfer occurs through the σ system.[22]

Spin-Selective Charge Transport Pathways. The energy level scheme depicted in Figure 1 shows that the CR within the singlet and triplet RP states give different products. The rates at which these products are formed and consequently their yields depend on two major considerations: (1) Spin dynamics controls the interconversion between the singlet and triplet RPs and determines population flow between the singlet and triplet manifolds. (2) The CR rates within the singlet and triplet manifolds depend on the electronic coupling matrix elements, V_{CRS} and V_{CRT}, as well as the Franck−Condon weighted density of states, which involves the reaction free energy and the total reorganization energy for CR. The rates and yields of singlet and triplet CR products in **1**−**5** are analyzed using these two basic ideas.

We have analyzed magnetic field dependent kinetic traces for **1**−**4** based on the radical pair mechanism with spin state dependent recombination reactions. For **1**−**3**, we have observed a distinct $2J$ resonance for both the triplet yield and the RP decay rate. The spin dynamics of the RP, where $2J$ is larger than the effective hyperfine interaction ($a_{eff} \sim 3\text{mT}$),[66,96] are described in Figure 11. For all cases, the initial RP population is localized only on the singlet state, and the kinetic equations used to obtain the fits are outlined in the Supporting Information. The CS kinetics are not considered because they are much faster than the CR kinetics and are not influenced by spin dynamics.

In the absence of a magnetic field (Figure 11A), the three triplet sublevels of the RP are nearly degenerate and are split from the singlet level by $2J$. Since the CR reactions are spin selective, the singlet RP exclusively recombines to the singlet ground state and the triplet RP recombines to the neutral triplet excited state with rate constants of k_{CRS} and k_{CRT}, respectively. Note that k_{CRT} is understood here as the sum of the recombination rates to ^{3*}NI and ^{3*}An. The detailed RP-ISC process at low fields for systems with large $2J$ has never been explicitly treated, but it is likely that the mixing process is governed by incoherent relaxation rather than coherent interconversion of the singlet and triplet RP states, considering the large energy gap ($2J$) and small hyperfine coupling.

At resonance (Figure 11B), where $B_0 = 2J$, the Zeeman splitting of triplet sublevels exactly matches $2J$, which makes

S degenerate with T_{+1} or T_{-1} for positive or negative J values, respectively. The polarization pattern of the SCRP spectra observed by TREPR reveals that J is positive regardless of n, which is not a factor in the kinetic analysis.[66] At resonance, S-T_{+1} mixing caused by the hyperfine interactions is considered to be coherent within the characteristic time scale of the effective hyperfine interaction, $a_{eff} \sim 10^8$ s^{-1}. This fast mixing can be described approximately as a kinetic equilibrium, if the other processes are slow relative to the mixing time scale.[97] At resonance, we also need to consider S-T and T-T relaxation processes.[98] For simplicity, we assume that the relaxation rates, k_{rlx}, are the same for S-T_0 and for single quantum T_0-$T_{\pm 1}$ relaxation as is the case at zero field. Double quantum relaxation and S-T_{-1} relaxation can be ignored considering the large energy gaps between the corresponding states. This approximation does not cause serious problems because the main population flows through fast S-T_{+1} mixing followed by recombination from both the S and T_{+1} states unless relaxation is very fast.

At high fields (Figure 11C), we can ignore the effect of S-$T_{\pm 1}$ and single quantum T-T relaxations. The valid limits of this treatment are confirmed by plotting the RP decay rate as a function of the applied field. According to current ideas regarding the relaxation mechanism,[98,99] k_{rlx} is slower at higher magnetic field, except when ultrahigh magnetic fields are applied.[100] The rate vs field plots for **1**−**4** (Figure 7) show flat features at high field, where the field dependent relaxation rate is much slower than the observed RP decay rate. Under these conditions, the only spin states involved are S and T_0, which are mixed by incoherent relaxation.

For **1**, the kinetics at zero field and at high field are almost the same, both of which show negligible triplet yield. This feature indicates that S-T_0 relaxation is much slower than the RP lifetime because $2J$ is very large and the radical pair lifetime is short. In this case, the mechanistic scheme simplifies; at magnetic fields far from resonance, the apparent decay rate of the RP should be identical to k_{CRS}. At resonance, the decay rate becomes $k_{obs} = k_{CRS}/2 + k_{CRT}/2$ because of fast interconversion only between S and T_{+1}. The monoexponential fits to the data for **1** at zero and high fields using the analytical solution for k_{obs} give almost identical values of k_{CRS} and k_{CRT} as described in Table 2 and Figure 10C. It is difficult to solve the equations describing the kinetics for **2** and **3** analytically, so we have solved them numerically using a matrix formalism.[97] We pick three kinetic traces: at zero field, at resonance, and at high field and fit them by simulation (Supporting Information, Figure S6). The parameters obtained by this method are summarized in Table 1. The rate constants k_{CRS} and k_{CRT} are obtained with a small error for both **2** and **3**. The relaxation rate constant k_{rlx} for **2** is slower than that for **3** (footnotes to Table 1), which is reasonable given that the energy gap is larger for **2** than for **3**. However, the detailed mechanism of S-T_0 relaxation is still an open question. One possibility could be the interplay of the hyperfine interaction and the very fast singlet−triplet dephasing

(96) Hayashi, H. *Introduction to Dynamic Spin Chemistry: Magnetic Field Effects upon Chemical and Biochemical Reactions*; World Scientific: Singapore, 2004.
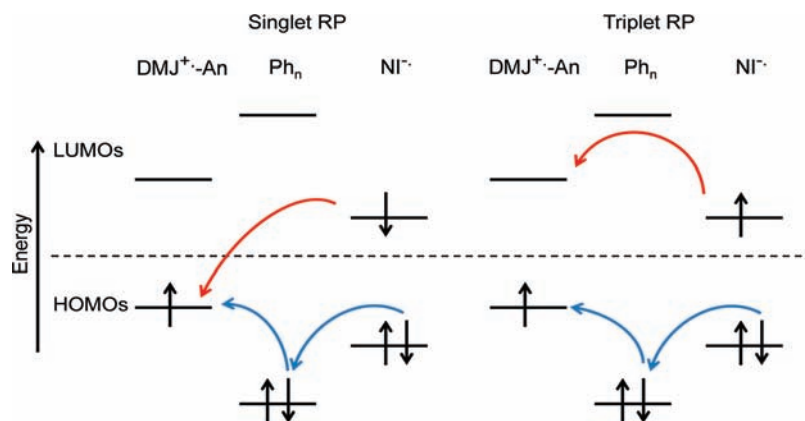
(97) Murakami, M.; Maeda, K.; Arai, T. *J. Phys. Chem. A* **2005**, *109* (26), 5793–5800.

(98) Hayashi, H.; Nagakura, S. *Bull. Chem. Soc. Jpn.* **1984**, *57* (2), 322–328.

(99) Carrington, A.; McLachlan, A. D. *Introduction to magnetic resonance with applications to chemistry and chemical physics*; Harper & Row: New York, 1967.

(100) Fujiwara, Y.; Aoki, T.; Yoda, K.; Cao, H.; Mukai, M.; Haino, T.; Fukazawa, Y.; Tanimoto, Y.; Yonemura, H.; Matsuo, T.; Okazaki, M. *Chem. Phys. Lett.* **1996**, *259* (3−4), 361–367.

Figure 12. Left: CR pathways for ^{1}(DMJ$^{+\bullet}$An-Ph$_n$-NI$^{-\bullet}$). Right: CR pathways for ^{3}(DMJ$^{+\bullet}$An-Ph$_n$-NI$^{-\bullet}$).

caused by fluctuations of the exchange interaction, $2J$.[101,102] These fluctuations could be a result of torsional motions about the single bonds joining each phenyl, as well as joining the bridge to the donor and acceptor.

For **4**, which shows a negligible resonance in its MFE plot due to the fact that $2J \ll a_{\text{eff}}$, the spin dynamics can be explained in terms of conventional hyperfine and relaxation mechanisms.[49,96] At zero field, all four RP states are completely mixed by the hyperfine interaction and the total rate is

$$k_{\text{obs}}(0\text{mT}) = \frac{1}{4}k_{\text{CRS}} + \frac{3}{4}k_{\text{CRT}} \qquad (8)$$

At high field, where the rate vs field plot is flat, only the S and T_0 states are fully mixed and the effect of relaxation between S-T_0 mixed state and $T_{\pm 1}$ state can be ignored. Thus, the rate becomes

$$k_{\text{obs}}(\text{high field}) = \frac{1}{2}k_{\text{CRS}} + \frac{1}{2}k_{\text{CRT}} \qquad (9)$$

The analytical solution of the two equations using the observed rates at zero and high fields gives k_{CRS} and k_{CRT} as shown in Table 1 and Figure 10C.

The similarity of the overall CR rates (k_{CR}) at zero field (Figure 11A) to those of k_{CRT} is explained by the spin dynamics of the RP, which is largely dependent on the $2J$ energy gap. When $2J$ is much larger than a_{eff} ($n = 1, 2$), CR occurs mainly by the singlet pathway because the singlet and triplet RP pair states interconvert slowly (see k_{rlx} for **2**). On the other hand, triplet CR predominates for **3** and **4** because of their smaller S-T energy gaps. Since S-T interconversion is faster than k_{CRS} (see k_{rlx} for **3**) and k_{CRT} is also fast, the value of overall rate constant k_{CR} is close to that of k_{CRT} rather than k_{CRS}. RP-ISC is governed by subtle spin interactions ($\ll$1 cm^{-1}) and thus can be the rate-determining step in the overall CR process when $2J$ is sufficiently large and the condition $k_{\text{CRS}} \ll k_{\text{rlx}} \ll k_{\text{CRT}}$ is fulfilled.

While spin dynamics governs the populations of singlet and triplet RPs, the subsequent CR reactions within these manifolds depend on the usual considerations of electron transfer theory.[93,94] The triplet CR ^{3}(DMJ$^{+\bullet}$-An-Ph$_n$-NI$^{-\bullet}$) → DMJ-An-Ph$_n$-^{3*}NI and DMJ-^{3*}An-Ph$_n$-NI occur within the normal region of the Marcus

(101) Miura, T.; Maeda, K.; Arai, T. *J. Phys. Chem. A* **2006**, *110* (12), 4151–4156.
(102) Miura, T.; Murai, H. *J. Phys. Chem. A* **2008**, *112* (12), 2526–2532.

rate vs free energy curve[103] because $|\Delta G_{\text{CRT}}| < 0.40$ eV and is faster than singlet CR ^{1}(DMJ$^{+\bullet}$-An-Ph$_n$-NI$^{-\bullet}$) → DMJ-An-Ph$_n$-NI, which occurs deep within the Marcus inverted region ($\Delta G_{\text{CRS}} = -2.1$ to -2.4 eV for $n = $ **1−5**).[9]

The separation of the rate constants for the singlet and triplet recombination pathways allows us to further determine the dominant charge transport mechanism as given by β, Figure 10C. The rate vs distance plots for the singlet and triplet pathways show that a superexchange mechanism prevails for CR with $\beta = 0.35$ Å^{-1} for k_{CRT} and $\beta = 0.48$ Å^{-1} for k_{CRS}. Since the triplet CR rates are similar to the total CR rates, it is reasonable that $\beta = 0.34$ Å^{-1} for the total CR rate as measured by the decay of NI$^{-\bullet}$ matches $\beta = 0.35$ Å^{-1} for the triplet pathway. This is also in agreement with the results obtained from the distance dependence of $2J$, where $\alpha = 0.36$ Å^{-1}, since eq 6 predicts $2J$ values that are dominated by the triplet pathway ($\Delta G_{\text{CRT}} + \lambda \ll \Delta G_{\text{CRS}} + \lambda$). The larger β value observed for the singlet CR pathway relative to that for the triplet pathway can be explained by considering the various electron transfer pathways available. For CR within ^{1}(DMJ$^{+\bullet}$An-Ph$_n$-NI$^{-\bullet}$), moving an electron via the HOMOs (Figure 12, left) must produce ^{1*}NI (blue arrows), whereas moving an electron via the LUMOs must produce either ^{1*}DMJ or the ground state of the system (red arrow). We do not observe ^{1*}NI, but we do observe CR to the ground state, so that singlet CR only involves the LUMOs. In contrast, considering CR for ^{3}(DMJ$^{+\bullet}$An-Ph$_n$-NI$^{-\bullet}$), moving an electron via the HOMOs (Figure 12, right) must produce ^{3*}NI (blue arrows), whereas moving an electron via the LUMOs must produce ^{3*}DMJ, which would undergo triplet−triplet energy transfer very rapidly to produce ^{3*}An (red arrow). We observe both ^{3*}NI and ^{3*}An following CR at 295 K, so that CR of the triplet RP to form ^{3*}NI involves the HOMOs, while CR to form ^{3*}An involves the LUMOs. Since superexchange involving the LUMOs has larger energy gaps, ΔE_{DB}, than does superexchange involving the HOMOs, eq 5 predicts that β will be larger for singlet CR than triplet CR, as we observe.

Temperature Dependence of Charge Recombination. As mentioned above, CR at 295 K initially produces both ^{3*}NI and ^{3*}An, while CR at 85 K produces ^{3*}NI preferentially. On the basis of the orbital discussion in the previous section, the room temperature result suggests that charge transfer uses both the HOMO and LUMO orbitals of the bridge, while the low temperature result suggests that charge transfer uses the HOMO

(103) Marcus, R. A. *J. Chem. Phys.* **1956**, *24*, 966–78.

orbitals leading to preferential production of ^{3*}NI. An examination of the data in Figure 5 shows that the DMJ-An-Ph$_n$$^{+\bullet}$-NI$^{-\bullet}$ virtual bridge states involving the bridge HOMOs have energies that are closer to those of DMJ$^{+\bullet}$-An-Ph$_n$-NI$^{-\bullet}$ than are the energies of the corresponding states DMJ$^{+\bullet}$-An-Ph$_n$$^{-\bullet}$-NI involving the bridge LUMOs. Thus, based on the energy gap dependence (ΔE_{DB}) given in eq 4, the electronic coupling for triplet CR (V_{CRT}) leading to ^{3*}NI should be somewhat larger than that leading to ^{3*}An. Using the functional form of the semiclassical expression for the electron transfer rate (eq 10),[93,94,104]

$$k_{CRT} = \frac{2\pi}{\hbar} |V_{CRT}|^2 \sqrt{\frac{1}{4\pi\lambda_s k_B T}} \sum_{n=0}^{\infty} e^{(-S)S^n/n!} e\left[-\frac{(\Delta G_{CRT} + \lambda_s + n\hbar\omega)^2}{4\lambda_s k_B T}\right] \quad (10)$$

where $\hbar\omega$ is the vibrational quantum, assumed to be 1500 cm^{-1} and $S = \lambda_i/\hbar\omega$, a larger value of V_{CRT} should result in a faster triplet CR rate. However, lowering the temperature to 85 K, at which toluene is a frozen glass, usually results in changes to ΔG_{CRT} and λ_s as well as V_{CRT}. We have demonstrated that restricting solvent dipole rotations by freezing the solvent results in large increases in ion pair energies.[105] These energies increase by as much as 0.75 eV relative to those obtained at room temperature in highly polar fluid media and about 0.2 eV above those obtained in liquid toluene. Moreover, since the frozen solvent behaves essentially as a low polarity medium, $\lambda_s \cong 0$ as determined from the Marcus treatment based on dielectric continuum theory.[103] Thus, given that λ_s is very small for CR in 1−5 in toluene at 295 K, λ_s is nearly temperature independent. Assuming that the ion pair energies of DMJ$^{+\bullet}$-An-Ph$_n$-NI$^{-\bullet}$, DMJ-An-Ph$_n$$^{+\bullet}$-NI$^{-\bullet}$ and DMJ$^{+\bullet}$-An-Ph$_n$$^{-\bullet}$-NI (Table S1) all increase by about 0.2 eV in glassy toluene at 85 K relative to their values determined in fluid toluene at 295 K, the corresponding values of ΔE_{DB} for the HOMO and LUMO superexchange pathways leading to ^{3*}NI and ^{3*}An, respectively, do not change, so that based on eq 4 V_{CRT} does not change, and the HOMO pathway is still favored. This analysis is supported by the fact that the TREPR measurements on DMJ$^{+\bullet}$-An-Ph$_n$-NI$^{-\bullet}$ in 4 and 5 show that 2J decreases only slightly as the temperature is lowered from 293 to 85 K (Figure 9, Table 1). Thus, the values of V_{CRT} for 4 and 5 only decrease by a small amount as the temperature decreases, most likely due to a reduction in the amplitude of torsional motions about the single bonds within the p-oligophenylene bridges.[83,106]

Despite the weak temperature dependence of V_{CRT}, an additional change in the relative rates of triplet CR leading to ^{3*}NI and ^{3*}An may result from the temperature dependence of the Franck−Condon weighted density of states (FCWD) term in eq 10. As noted above, the values of ΔG_{CRT} for the CR reactions that produce ^{3*}NI and ^{3*}An from ^{3}(DMJ$^{+\bullet}$-An-Ph$_n$-NI$^{-\bullet}$) become more negative as the temperature is lowered, largely as a consequence of destabilization of the ion pair state upon freezing the solvent.[105] For example, for ^{3}(DMJ$^{+\bullet}$-An-Ph$_2$-NI$^{-\bullet}$) → DMJ-An-Ph$_2$-^{3*}NI, $\Delta G_{CRT} = -0.22$ eV at 295 K and -0.42 at 85 K, while for ^{3}(DMJ$^{+\bullet}$-An-Ph$_2$-NI$^{-\bullet}$) → DMJ-An-Ph$_2$-^{3*}An, $\Delta G_{CRT} = -0.40$ eV at 295 K and -0.60 eV at 85 K. Using these values of ΔG_{CRT}, $\lambda_i = 0.39$ eV, and $\lambda_S = 0.07$ eV; and assuming that V_{CRT} is the same at both 295 and 85 K, eq 10 yields $k_{CRT}^{NI}/k_{CRT}^{An} = 1.0$ at 295 K and $k_{CRT}^{NI}/k_{CRT}^{An} = 1.7$ at 85 K. Thus, for 2 at room temperature, CR recombination to ^{3*}NI and ^{3*}An proceed at similar rates, while at 85 K CR to ^{3*}NI is nearly twice as fast as CR to ^{3*}An. This agrees with our previous TREPR results at 85 K, which show a preference of hole transfer to initially form ^{3*}NI, rather than electron transfer to form ^{3*}An, as well as our room temperature results presented here, which do not show a strong preference.

Conclusions

We have prepared a series of D-B-A molecules to understand the charge transport properties in simple bridging structures consisting of p-oligophenylenes ($n = 1-5$) covalently attached to a DMJ-An donor and an NI acceptor. We have determined how the electronic coupling depends on molecular structure by analyzing the spin−spin exchange interaction (2J) between the unpaired spins of the radical pair as determined by magnetic field effects on triplet and radical ion pair yields as well as time-resolved EPR spectroscopy and have established that the distance dependence of charge recombination in D-B-A molecules is spin-selective using magnetic field effect data and a kinetic model to separate the spin-selective charge recombination rates, k_{CRS} and k_{CRT}. The spin dynamics between the radical ion pairs and the electron transfer parameters within each spin manifold combine to strongly favor triplet charge recombination that results in the formation of both ^{3*}An and ^{3*}NI. An analysis of these phenomena in the context of superexchange theory leads us to identify participation of the bridge HOMOs in the formation of ^{3*}NI, while participation of the bridge LUMOs leads to formation of ^{3*}An. A similar analysis also explains why charge recombination leads preferentially to ^{3*}NI formation at low temperatures and comparable amounts of ^{3*}NI and ^{3*}An at room temperature. Interestingly, the structural and electronic impact of An integrated within the p-oligophenylene bridge does not significantly change the donor−acceptor electronic coupling within this system. These results show that once CS has occurred, An behaves like Ph with the bridge. It is possible that the dihedral angles between An and Ph$_n$ are sufficiently large that the propagation of electronic coupling through the An-Ph$_n$ bridge involves both the σ and π systems of An.

Developing systems for solar energy conversion and organic electronics requires a thorough knowledge of the dependence of charge transport properties on molecular structure. In addition, the results presented here show that the spin dynamics of the system provide an important tool for understanding charge transport mechanisms as well as a potential means of controlling long-distance charge transport in organic materials.

Supporting Information Available: Details regarding the synthesis and characterization of 5, and additional redox, transient absorption, and magnetic field effect data. This material is available free of charge via the Internet at http://pubs.acs.org.

(104) Hopfield, J. J. *Proc. Natl. Acad. Sci. U.S.A.* **1974**, *71*, 3640–3644.
(105) Gaines, G. L., III; O'Neil, M. P.; Svec, W. A.; Niemczyk, M. P.; Wasielewski, M. R. *J. Am. Chem. Soc.* **1991**, *113* (2), 719–21.
(106) Berlin, Y. A.; Grozema, F. C.; Siebbeles, L. D. A.; Ratner, M. A. *J. Phys. Chem. C* **2008**, *112* (29), 10988–11000.

JA907625K